

SDSS-IV MANGA: THE INTRINSIC SHAPE OF SLOW ROTATOR EARLY-TYPE GALAXIES

HONGYU LI (李弘宇)^{1,2} SHUDE MAO,^{3,1,4} MICHELE CAPPELLARI,⁵ MARK T. GRAHAM,⁵ ERIC EMSELLEM,^{6,7} AND
R. J. LONG^{1,4}

¹*National Astronomical Observatories, Chinese Academy of Sciences, 20A Datun Road, Chaoyang District, Beijing 100012, China*

²*University of Chinese Academy of Sciences, Beijing 100049, China*

³*Physics Department and Tsinghua Centre for Astrophysics, Tsinghua University, Beijing 100084, China*

⁴*Jodrell Bank Centre for Astrophysics, School of Physics and Astronomy, The University of Manchester, Oxford Road, Manchester M13 9PL, UK*

⁵*Sub-Department of Astrophysics, Department of Physics, University of Oxford, Denys Wilkinson Building, Keble Road, Oxford, OX1 3RH, UK*

⁶*Université Lyon 1, Observatoire de Lyon, Centre de Recherche Astrophysique de Lyon and Ecole Normale Supérieure de Lyon, 9 avenue Charles André, F-69230 Saint-Genis Laval, France*

⁷*European Southern Observatory, Karl-Schwarzschild-Str. 2, 85748 Garching, Germany*

Submitted to ApJ Letters

ABSTRACT

By inverting the distributions of galaxies' apparent ellipticities and misalignment angles (measured around the projected half-light radius R_e) between their photometric and kinematic axes, we study the intrinsic shape distribution of 189 slow rotator early-type galaxies with stellar masses $2 \times 10^{11} M_\odot < M_* < 2 \times 10^{12} M_\odot$, extracted from a sample of about 2200 galaxies with integral-field stellar kinematics from the DR14 of the SDSS-IV MaNGA IFU survey. Thanks to the large sample of slow rotators, Graham+18 showed that there is clear structure in the misalignment angle distribution, with two peaks at both 0° and 90° misalignment (characteristic of oblate and prolate rotation respectively). Here we invert the observed distribution from Graham+18. The large sample allows us to go beyond the known fact that slow rotators are weakly triaxial and to place useful constraints on their intrinsic triaxiality distribution (around $1R_e$) for the first time. The shape inversion is generally non-unique. However, we find that, for a wide set of model assumptions, the observed distribution clearly requires a dominant triaxial-oblate population. For some of our models, the data suggest a hint for a minor triaxial-prolate population, but a dominant prolate population is ruled out.

Keywords: Galaxy: kinematics and dynamics — Galaxy: structure — Galaxy: evolution

arXiv:1807.08872v1 [astro-ph.GA] 24 Jul 2018

1. INTRODUCTION

The intrinsic shape distribution of early-type galaxies has been studied for decades by statistically inverting the distribution of their ellipticities (e.g. Sandage et al. 1970; Binney & de Vaucouleurs 1981; Fasano & Vio 1991; Lambas et al. 1992; Ryden 1992; Kimm & Yi 2007) or the distribution of their ellipticities and misalignment angles between photometric and kinematic axes (e.g. Weijmans et al. 2014; Foster et al. 2017). Although the recovered intrinsic shape distributions from such methods are in general non-unique (Franx et al. 1991), the fact that all the fast rotators have kinematic axes aligned with their photometric axes (Cappellari et al. 2007; Emsellem et al. 2007; Krajnović et al. 2011; Fogarty et al. 2015) can only be explained if, as a class, they are nearly axisymmetric (with or without bars). For slow rotators, however, the two axes can be misaligned. Previous studies show that slow rotators are weakly triaxial (Weijmans et al. 2014; Foster et al. 2017), but it is difficult to see any significant features of the misalignment angle distribution due to their limited sample sizes. A more detailed review on this topic can be found in section 3.3 of Cappellari (2016).

In recent cosmological hydrodynamic simulations (e.g. fig. 7 of Schaller et al. 2015, fig.10 of Li et al. 2016, Velliscig et al. 2015 and Li et al. 2018a), many massive galaxies are found to be prolate-like, manifesting as mostly slow rotators with different kinematic misalignment angles and formed by major mergers with radial orbits (Li et al. 2018a). This theory is broadly consistent with the observation that genuine kinematic misalignment between photometry and kinematics, including some nearly 90-degree misalignments (Krajnović et al. 2011), only happens in slow rotators, which are found above a characteristic stellar mass ($M_{\text{crit}} \approx 2 \times 10^{11} M_{\odot}$; e.g. fig. 11 of Emsellem et al. 2011; Cappellari et al. 2013a; Cappellari 2016). It would be useful to study the intrinsic shape distribution of slow rotators observationally and put constraints on galaxy formation models.

Some recent works have interpreted the existence of a handful of massive galaxies with 90-degree misalignment as circumstantial evidence for the existence of prolate galaxies, e.g. in the CALIFA survey Tsatsi et al. (2017) and the MUSE Most Massive Galaxies (M3G) survey (Krajnović et al. 2018). Especially in the M3G survey, half of the massive ($M > 10^{12} M_{\odot}$) galaxies have 90-degree misalignments. However a 90-degree misalignment is also naturally expected as a significant fraction for triaxial galaxies (see e.g. this paper). This implies that, unless all slow rotators were 90-degree misaligned, which is not the case (see fig.6 of Cappellari 2016), one cannot interpret 90-degree misalignments as evidence for prolate galaxies. Conclusions on galaxy shapes cannot be reached without a statistical study but the number statistics are so far too limited for this kind of analysis.

MaNGA (Bundy et al. 2015) is currently the largest IFU survey observed by the 2.5m Sloan Telescope (Gunn et al. 2006), and as reported by Graham et al. (2018), provides a sufficiently large number of slow rotators to detect actual structure in the distribution of kinematic misalignments. In this Letter we analyze the distributions of ellipticity and misalignment angle measured around the effective radius to provide the first statistical study of the shape distribution of slow rotators, and goes beyond the well-established fact that they are “weakly triaxial” (e.g. review by Cappellari 2016).

The structure of this Letter is as follows. In Section 2, we introduce the galaxy sample and the methods we use. In Section 3, we show the results. In Section 4, we summarize our results and draw conclusions.

2. SAMPLE AND METHODS

2.1. Sample selection and data

We use the galaxy sample from Graham et al. (2018), based on SDSS-IV DR14 MaNGA (Abolfathi et al. 2017), which has ~ 2700 galaxies. The measured ellipticity ε , misalignment angle Ψ_{mis} (around the effective radius), beam-corrected angular momentum parameter λ_{R_e} and kinematic classification are from table 2 of Graham et al. (2018). We select massive slow rotators using two alternative techniques. The first is quantitative: we select galaxies with $\lambda_{R_e} < 0.08 + \varepsilon/4$ and $\varepsilon < 0.4$ (Cappellari 2016), as indicated by the black solid lines in fig. 11 of Graham et al. (2018). The second one is qualitative: we select galaxies with visually-classified ETGs as non-regular rotators. These galaxies do not exhibit a spider diagram velocity map and this is thought to be an indicator of a slow rotator (see Graham et al. 2018 and fig. 4 of Cappellari 2016 for more details). In both samples, we remove galaxies with $M \equiv 2 \times M_{1/2} < 2 \times 10^{11} M_{\odot}$, where $M_{1/2}$ is the dynamical mass within the 3-dimensional half-light radius ($r_{1/2}$) from table 1 of Li et al. (2018b). When the dark matter is small within the effective radius, M defined above is a good proxy of the stellar mass (Cappellari et al. 2013b). This cut on mass is needed because most slow or non-regular rotators with $M < 2 \times 10^{11} M_{\odot}$ are not genuine slow rotators (Graham et al. 2018). Finally, we have 189 galaxies in the slow rotator sample and 74 galaxies in the non-regular sample. We note here that 72 of the 74 non-regular rotators are also in the 189 slow rotator sample.

In Fig. 1, we show the 1D histograms and the 2D distribution of the observed ellipticity ε and kinematic misalignment ψ_{mis} for slow rotators and non-regular rotators from Graham et al. (2018). We shift and symmetrize the misalignment angle distribution. We note that we did not modify the data values in the symmetrization but just plot the data twice between $[-90^{\circ}, 0^{\circ}]$ and $[0^{\circ}, 90^{\circ}]$ for clearer visualisation. In the model fitting, we still use the original distribution as

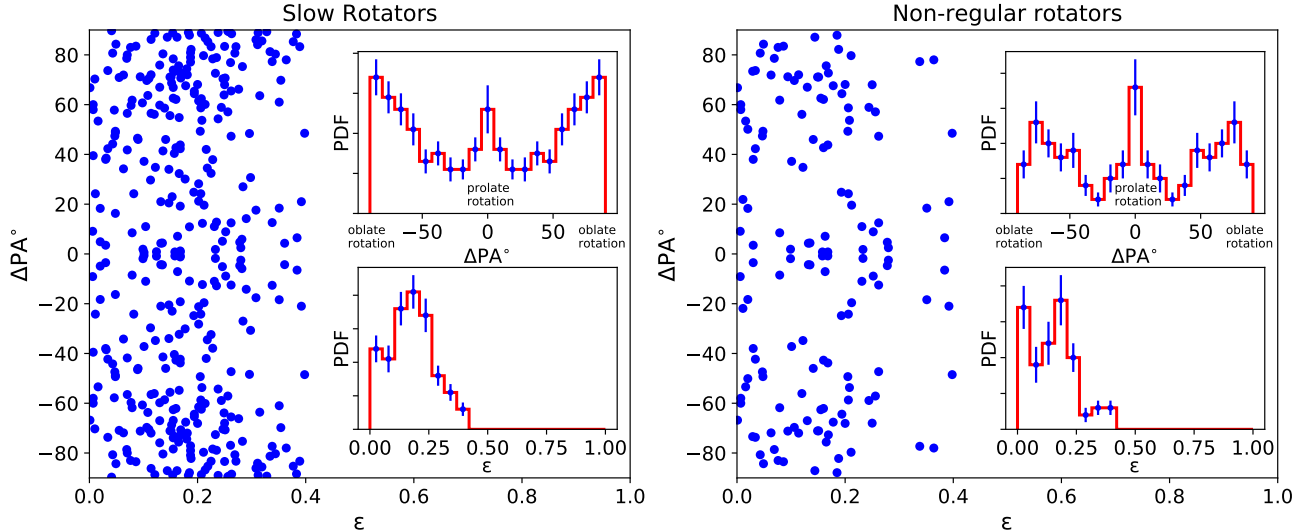


Figure 1. The observed distribution of ellipticity ε and kinematic misalignment ΔPA for slow rotators (left) and non-regular rotators (right). For clearer visualisation, we shift the kinematic misalignment angle ψ_{mis} by 90° and symmetrize their values about 0° , i.e. $|\Delta PA| = 90^\circ - |\psi_{\text{mis}}|$. By doing this, the peak around the prolate rotation can be clearly seen at the centre of the distribution, i.e. $\Delta PA = 0^\circ$. In each panel, every blue dot represents an observed galaxy, the red histograms show their 1D distribution, and the blue error bars show the error estimated using the bootstrapping method.

input. For normal axisymmetric rotation, $\Delta PA = \pm 90^\circ$. The uncertainties estimated by the bootstrapping method are shown by the blue error bars. As one can see, the peak around $\Delta PA = 0^\circ$ has a confidence level more than two-sigma.

2.2. Projection of luminosity density and velocity field

The projection of the luminosity density of a triaxial galaxy has been discussed in Stark (1977), Binney (1985) and Franx (1988). Here we just make a brief summary. Following Binney (1985), we assume the luminosity density of a triaxial galaxy could be described by similar coaxial ellipsoids, i.e. $\rho = \rho(m^2)$, where $m^2 = x^2/a^2 + y^2/b^2 + z^2/c^2$, and x -, y - and z -axes are aligned with the principal axes with $a > b > c$. The axis ratios are defined as

$$\zeta = b/a, \quad \xi = c/a, \quad \eta = c/b. \quad (1)$$

When a galaxy is viewed along the direction (θ, ϕ) in polar coordinates, the projected ellipticity ε and the minor axes position angle Γ_{minor} with respect to the projected z -axis are completely determined by the intrinsic axes ratios (equations 12 and 13 in Binney 1985)

$$\varepsilon(\theta, \phi; \xi, \zeta) = 1 - \sqrt{\frac{A + C - \sqrt{(A - C)^2 + B^2}}{A + C + \sqrt{(A - C)^2 + B^2}}}, \quad (2)$$

$$\Gamma_{\text{minor}}(\theta, \phi; \xi, \zeta) = \frac{1}{2} \arctan\left(\frac{B}{A - C}\right), \quad (3)$$

with

$$A \equiv \frac{\cos^2 \theta}{\xi^2} \left(\sin^2 \phi + \frac{\cos^2 \phi}{\zeta^2} \right) + \frac{\sin^2 \theta}{\zeta^2}, \quad (4)$$

$$B \equiv \cos \theta \sin 2\phi \left(1 - \frac{1}{\zeta^2} \right) \frac{1}{\xi^2}, \quad (5)$$

$$C \equiv \left(\frac{\sin^2 \phi}{\zeta^2} + \cos^2 \phi \right) \frac{1}{\xi^2}. \quad (6)$$

In a triaxial galaxy, the angular momentum vector is not required to be aligned with the principal axes, but can lie anywhere in the $x - z$ plane (Statler 1987). Following Franx et al. (1991), we define $0^\circ \leq \psi_{\text{int}} \leq 90^\circ$ as the angle between the z -axis and the angular momentum vector. The position angle of the apparent angular momentum Γ_{kin} with respect to the projected z -axis only depends on the viewing angle and the intrinsic misalignment (equation 6 in Franx et al. 1991)

$$\tan \Gamma_{\text{kin}} = \frac{\sin \phi \sin \psi_{\text{int}}}{-\cos \phi \cos \theta \sin \psi_{\text{int}} + \sin \theta \cos \psi_{\text{int}}}. \quad (7)$$

The kinematic misalignment angle Ψ between the projected minor axis and the projected angular momentum is given by

$$\sin \Psi = |\sin(\Gamma_{\text{kin}} - \Gamma_{\text{minor}})|, \quad 0^\circ \leq \Psi \leq 90^\circ, \quad (8)$$

where Ψ corresponds to our observed quantity $|\psi_{\text{mis}}|$ from Graham et al. (2018).

2.3. Monte Carlo simulations

From Section 2.2, we know the apparent kinematic misalignment angle Ψ and apparent ellipticity ε are determined by the intrinsic axis ratios (ζ, ξ) , intrinsic misalignment angle of the angular momentum ψ_{int} and viewing angle (θ, ϕ) , i.e. $\Psi = \Psi(\zeta, \xi, \psi_{\text{int}}, \theta, \phi)$,

$\varepsilon = \varepsilon(\zeta, \xi, \theta, \phi)$. If we assume the viewing angle is random (i.e. flat distributions in $[-1, 1]$ for $\cos\theta$ and $[0, 2\pi]$ for ϕ), and the distribution of the axis ratios and intrinsic misalignment of the galaxies in our sample can be described by some distribution functions, e.g. $p(\zeta)$, $p(\xi) = p(\xi/\zeta|\zeta)p(\zeta) = p(\eta|\zeta)p(\zeta)$ and $p(\psi_{\text{int}})$, we can calculate the model probability distribution of Ψ and ε

$$p(\Psi, \varepsilon) = p[\Psi, \varepsilon | p(\zeta), p(\eta), p(\psi_{\text{int}})] \quad (9)$$

The reason for using $p(\eta)$ instead of $p(\xi)$ is because η is between 0 and 1 and is independent of ζ , which makes it easier and faster to implement numerically, while ξ has to be smaller than ζ . We also confirmed by visual examination that the distribution $p(\xi)$ derived from $p(\zeta)$ and $p(\eta)$ in our model is physically reasonable and can cover various shapes of distributions.

We use two different models to parameterize $p(\zeta)$, $p(\eta)$ and $p(\psi_{\text{int}})$. The first one is a single-population model, in which we assume $p(\zeta)$, $p(\eta)$ and $p(\psi_{\text{int}})$ are independent and can be described by single truncated Gaussian functions

$$p(\zeta|\mu_\zeta, \sigma_\zeta) \propto \frac{1}{\sqrt{2\pi\sigma_\zeta^2}} \exp\left(-\frac{(\zeta - \mu_\zeta)^2}{\sigma_\zeta^2}\right), \quad 0 \leq \zeta \leq 1 \quad (10)$$

$$p(\eta|\mu_\eta, \sigma_\eta) \propto \frac{1}{\sqrt{2\pi\sigma_\eta^2}} \exp\left(-\frac{(\eta - \mu_\eta)^2}{\sigma_\eta^2}\right), \quad 0 \leq \eta \leq 1 \quad (11)$$

$$p(\psi_{\text{int}}|\mu_{\psi_{\text{int}}}, \sigma_{\psi_{\text{int}}}) \propto \frac{1}{\sqrt{2\pi\sigma_{\psi_{\text{int}}}^2}} \exp\left(-\frac{(\psi_{\text{int}} - \mu_{\psi_{\text{int}}})^2}{\sigma_{\psi_{\text{int}}}^2}\right), \quad 0 \leq \psi_{\text{int}} \leq \frac{\pi}{2} \quad (12)$$

The probability outside the boundary is truncated and set to 0. There are 6 free parameters for a single-population model, they are μ_ζ , σ_ζ , μ_η , σ_η , $\mu_{\psi_{\text{int}}}$ and $\sigma_{\psi_{\text{int}}}$.

The second model is a two-population model, in which we assume $p(\zeta)$, $p(\eta)$ and $p(\psi_{\text{int}})$ are independent and can be described by two truncated Gaussian functions, with each Gaussian representing a galaxy population (e.g. oblate, triaxial or prolate)

$$p(\zeta|\mu_{\zeta_1}, \sigma_{\zeta_1}, \mu_{\zeta_2}, \sigma_{\zeta_2}) = f_1 p(\zeta|\mu_{\zeta_1}, \sigma_{\zeta_1}) + (1 - f_1) p(\zeta|\mu_{\zeta_2}, \sigma_{\zeta_2}), \quad (13)$$

$$p(\eta|\mu_{\eta_1}, \sigma_{\eta_1}, \mu_{\eta_2}, \sigma_{\eta_2}) = f_1 p(\eta|\mu_{\eta_1}, \sigma_{\eta_1}) + (1 - f_1) p(\eta|\mu_{\eta_2}, \sigma_{\eta_2}), \quad (14)$$

$$p(\psi_{\text{int}}|\mu_{\psi_{\text{int}_1}}, \sigma_{\psi_{\text{int}_1}}, \mu_{\psi_{\text{int}_2}}, \sigma_{\psi_{\text{int}_2}}) = f_1 p(\psi_{\text{int}}|\mu_{\psi_{\text{int}_1}}, \sigma_{\psi_{\text{int}_1}}) + (1 - f_1) p(\psi_{\text{int}}|\mu_{\psi_{\text{int}_2}}, \sigma_{\psi_{\text{int}_2}}). \quad (15)$$

where f_1 represents the fraction of the galaxies in the first galaxy population. The functional form and truncation boundary for each population are exactly the same as in equations 10, 11 and 12. There are 13 free parameters in this model, they are μ_{ζ_1} , σ_{ζ_1} , μ_{η_1} , σ_{η_1} , $\mu_{\psi_{\text{int}_1}}$, $\sigma_{\psi_{\text{int}_1}}$, μ_{ζ_2} , σ_{ζ_2} , μ_{η_2} , σ_{η_2} , $\mu_{\psi_{\text{int}_2}}$, $\sigma_{\psi_{\text{int}_2}}$ and f_1 .

In the models above, we assume the intrinsic misalignment is independent of the intrinsic shape. However, a one-to-one relation is assumed in previous studies (Weijmans et al. 2014; Foster et al. 2017)

$$\tan \psi_{\text{int}} = \sqrt{\frac{T}{1-T}}, \quad (16)$$

where $T = \frac{a^2 - b^2}{a^2 - c^2}$ is the triaxial parameter (i.e. the intrinsic shape). We also adapt this one-to-one relation in our single- and two-population models in our Monte Carlo simulations. In summary, the models we use are

1. a single-population model with independent intrinsic misalignment, 6 free parameters;
2. a two-population model with independent intrinsic misalignment, 13 free parameters;
3. a single-population model with intrinsic misalignment following the model of Weijmans et al. (2014), 4 free parameters;
4. a two-population model with intrinsic misalignment following the model of Weijmans et al. (2014), 9 free parameters.

For all the models, we estimate $p(\Psi, \varepsilon)$ in equation 9 numerically. With a given set of model parameters \vec{p} , we first sample n points of $\cos\theta$, ϕ from a flat distribution, and ζ , η and ψ_{int} from $p(\zeta|\vec{p})$, $p(\eta|\vec{p})$ and $p(\psi_{\text{int}}|\vec{p})$, respectively (for the Weijman+14 models, ψ_{int} is calculated directly using equation 16). We then calculate the model predicted ε and Ψ for every point using equation 2 and 8 respectively, and bin all the points on a 2-dimensional histogram (25 by 25). Finally, we normalise the histogram, and use bilinear interpolation to calculate the probability for a given (Ψ, ε) . We set $n = 9,000,000$ in our calculation, which is enough to produce a smooth probability distribution.

We perform the inversion, i.e. infer $p(\zeta)$, $p(\xi)$ and $p(\psi_{\text{int}})$ from the observed distribution, by maximizing the likelihood of the observed distribution, defined as

$$\ln L = \sum_i \ln p(|\psi_{\text{mis}}^i|, \varepsilon_i) \quad (17)$$

where ψ_{mis}^i and ε_i are the apparent kinematic misalignment angle and ellipticity for the i -th observed galaxy. $p(\Psi, \varepsilon)$ is defined in equation 9 and estimated numerically using the method described above. The sum is over all the galaxies in the sample (i.e. slow rotators or non-regular rotators described in Section 2.1). We use a python implementation of the MCMC algorithm (**emcee**, Foreman-Mackey et al. 2013) to obtain the parameters which maximize the likelihood as well as the probability distribution of the model parameters. We use 200 walkers and run for 3000 and 12000 steps for the single-population model and two-population model, respectively. In addition to **emcee**, we also tried another MCMC package **AdaMet** (Cappellari et al. 2013b). Those two packages give similar results. The parameters are sampled within their mathematical limits. For the single-population model, they are: $[0, 1]$ for μ_ζ and μ_η ; $[0, 1]$ for σ_ζ and σ_η ; $[0, \pi/2]$ for $\mu_{\psi_{\text{int}}}$; $[0, \frac{3}{2}\pi]$ for $\sigma_{\psi_{\text{int}}}$. For the two-population model, the boundaries are $[0, 1]$ for μ_{ζ_1} , μ_{η_1} , μ_{ζ_2} and μ_{η_2} ; $[0, 1]$ for σ_{ζ_1} , σ_{η_1} , σ_{ζ_2} and σ_{η_2} ; $[0, \pi/2]$ for $\mu_{\psi_{\text{int}_1}}$ and $\mu_{\psi_{\text{int}_2}}$; $[0, \pi/2]$ for $\sigma_{\psi_{\text{int}_1}}$ and $\sigma_{\psi_{\text{int}_2}}$; $[0, 1]$ for f_1 .

3. RESULTS

In this section, we show the fitting results of the observed distribution for all the models. To test the robustness of our results, we fit both the slow rotator samples selected with different techniques in Section 2.1. The fitting is performed using the methods described in Section 2.3.

The model which maximizes the likelihood and the probability distribution function (PDF) from MCMC for the single-population model with independent intrinsic misalignment is shown in Fig. 2. From the probability distribution (blue histograms) in the left panels, the model can produce 3 peaks (around $\Delta PA = 0^\circ, \pm 90^\circ$), which qualitatively agree with the observed data. However, the model fits the detailed structures less well, e.g. the dip between $\sim 20^\circ$ and $\sim 40^\circ$, especially for non-regular rotators. Furthermore, in the right panels, one can see that the model predicted axis ratios from different samples do not agree with each other: galaxies in the slow rotator sample prefer a triaxial-oblate shape with a flat intrinsic misalignment distribution while galaxies in the non-regular sample prefer a triaxial-prolate shape with flat intrinsic misalignment.

Similar diagrams for the two-population model with independent intrinsic misalignment are shown in Fig. 3. As can be seen from the probability distribution (blue histogram) in the left panels, the model can not only give 3 peaks, but also match the amplitude of the peaks and other detailed structures relatively well. We also calculate the p-value from the KS statistic for the 1D distribution of ΔPA . We find that the p-value increases from ~ 0.8 to ~ 1 after we change to the two-population model. From the probability distribution of the axis ratio distributions (blue histogram and con-

tours) in the right panels, the galaxy sample is dominated by a triaxial-oblate population, while there are also some minor galaxy populations located in other regions. But due to large model degeneracy, it is difficult to constrain their axis ratios well. We note that in practice it is difficult for the MCMC chain to converge under such large model degeneracy, unless it is run with extremely long steps. In general, the probability distributions of intrinsic axis ratios are similar for slow rotators and non-regular rotators, despite the different selection criteria.

In Fig. 4, we show the results of single- and two-population models with Weijmans+14 intrinsic misalignment for the slow rotator sample. Unlike the independent intrinsic misalignment model in Fig. 2, the single-population model with Weijmans+14 intrinsic misalignment fails to reproduce the observed peaks. In order to explain the observations, the model requires $\sim 70\%$ of the galaxies in the sample have triaxial-oblate shape while the other $\sim 30\%$ have triaxial-prolate shape. Although model dependent, this gives us a hint that there might be a minor population in the slow rotators which has triaxial-prolate shape. The best-fit model parameters and their uncertainties from MCMC are listed in Table 1.

In order to test whether our results are affected by outliers (e.g. galaxies with no rotation or poor data qualities), we rerun our model including an outlier component with constant likelihood. The results are still the same and the outlier fraction (free parameter in the fitting) is less than 5% for all the models and samples. We also try a different axis ratio parametrization described in Lambas et al. (1992). The conclusions remain unchanged.

4. CONCLUSIONS

We study the distribution of apparent ellipticity and kinematic misalignment for slow rotators measured in Graham et al. (2018), based on a SDSS-IV DR14 MaNGA sample. The distribution shows clear structure in the misalignment angle distribution: there are two peaks at both 0° and 90° misalignment (characteristic of oblate and prolate rotation respectively). By assuming Gaussian shapes of the axis ratios and the intrinsic misalignment distribution, we invert the observed distribution to obtain the intrinsic one using Monte Carlo simulations.

We find that our models with different assumptions clearly requires a dominant triaxial-oblate population, beyond the known fact that slow rotators are weakly triaxial. If we assume the intrinsic shape and the intrinsic misalignment are independent, the constraints on the intrinsic axis ratios are less strong. The observed distribution can be explained by a dominant triaxial-oblate population (with some minor populations of different shapes). However, if a one-to-one intrinsic shape-misalignment relation is assumed, the model re-

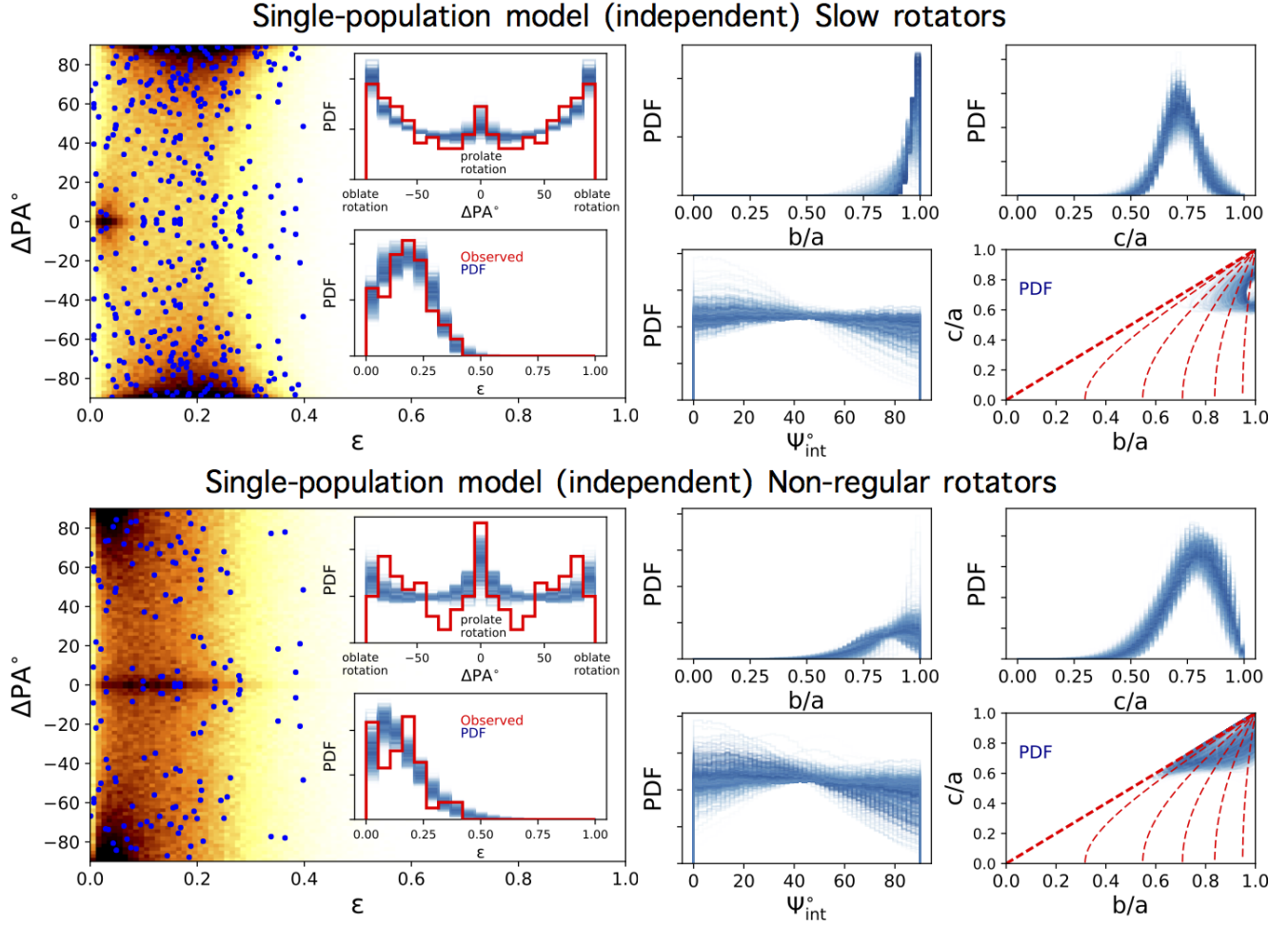


Figure 2. Single-population models with independent intrinsic misalignment for massive slow rotators classified using two alternative techniques, namely either (i) from the $(\lambda_{Re}, \varepsilon)$ diagram (top) or (ii) visually classified from their kinematic maps (bottom). In each left panel, the blue dots show the observed distribution, and the colour map shows the model distribution which maximizes the likelihood. The red histograms show the observed distribution. The blue lines show the probability distribution, which are randomly selected from the MCMC chain and colour coded by their likelihood. The bluer the colour, the larger the likelihood. We use the same method described in Fig. 1 to shift and symmetrize the distribution for visualisation purposes only. We note that we still use the original distribution in the model fitting process. The predicted axis ratio and intrinsic misalignment are shown by the blue lines in the right panels. In the b/a vs. c/a panel (lower right), every blue line shows the 1σ (68%) contour of the 2D axis ratio distribution of that model. The red thin-dashed lines, from left to right, show the line of constant triaxial parameter $T = \frac{a^2 - b^2}{a^2 - c^2}$: 0.1, 0.3, 0.5, 0.7 and 0.9. The red thick-dashed line shows the position where the axis ratio $b/a = c/a$.

quires two distinct galaxy populations (i.e. a dominant triaxial-oblate population and a minor triaxial-prolate population) in order to explain the observations, suggesting a hint for a minor triaxial-prolate population.

The uncertainties in our study mainly come from the observational uncertainties of the misalignment angle and the ellipticity plus the intrinsic degeneracies in the inversion problem. In the study, we measure the ellipticity, photometric and kinematic position angles around the effective radius, and these values could vary with radius and cause uncertainties in the analysis. In addition, galaxies with round shape and very slow rotation

have large uncertainties in the misalignment angle measurement. These uncertainties are difficult to estimate robustly and incorporate in the model. Better observations and larger samples may help to reduce these uncertainties as well as the Poisson noise shown in Fig. 1. The model degeneracies are intrinsic and difficult to remove. Our simulations show that the fitting results depend on the intrinsic misalignment model. This suggests a better understanding of the intrinsic shape-misalignment relationship can be useful in the inversion. A study in numerical simulation may be helpful. The MaNGA sample we used is not volume limited, but has a flat stellar mass

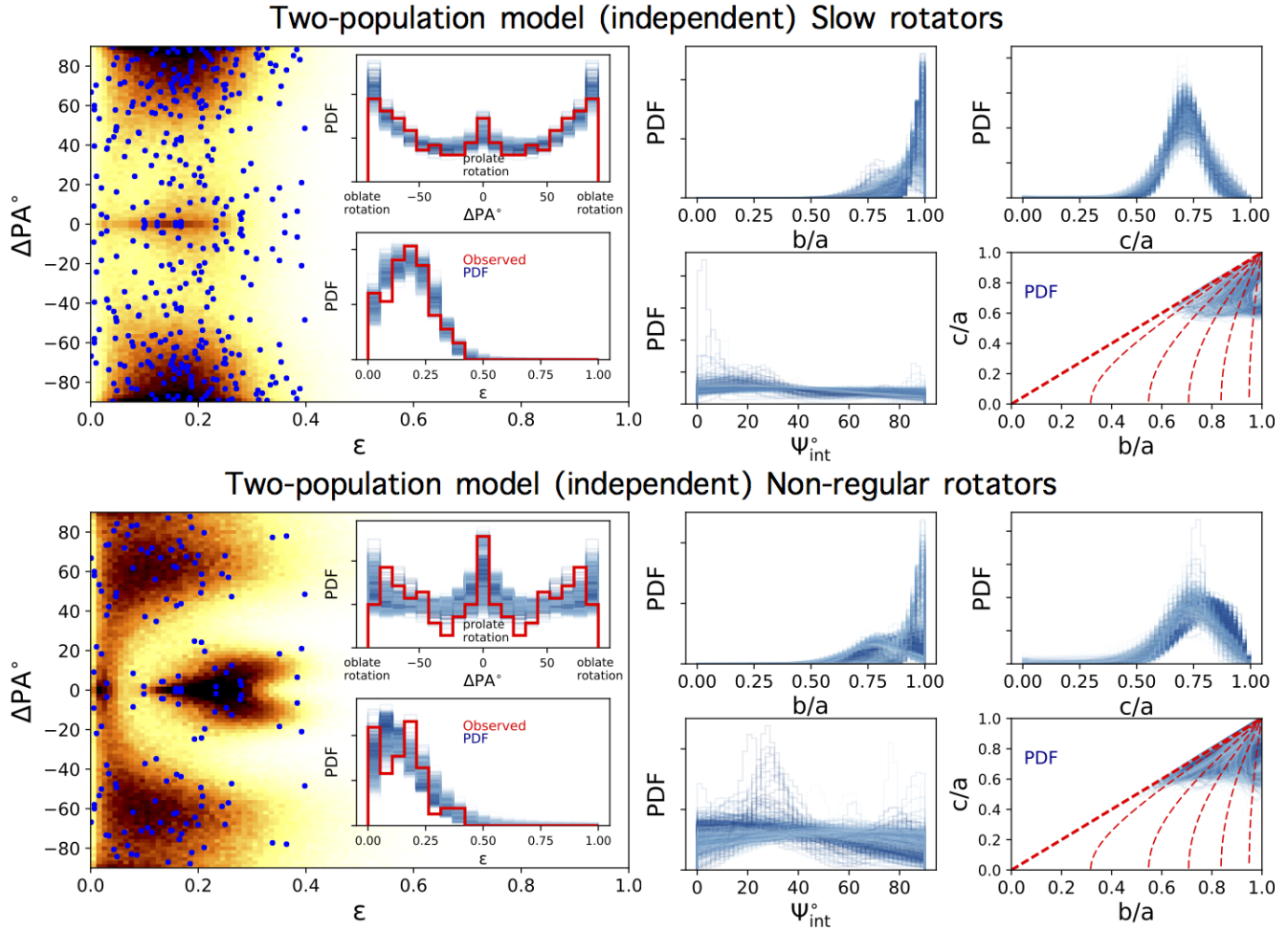


Figure 3. Two-population model with independent intrinsic misalignment for slow rotators (top) and non-regular rotators (bottom). The other labels and legends are the same as Fig. 2.

Table 1. Best-fit (maximum likelihood) parameters for the models shown in Figs. 2, 3 and 4. The uncertainties are calculated as the differences between the 16th and 50th, 50th and 84th percentiles (1σ) of the 1D distribution of each parameter, respectively. We note that the best-fit parameters can deviate from the 50th percentile (i.e. the median), since the posterior distributions are irregular. SR and NR represent slow rotators and non-regular rotators. SINGLE-INDEPENDENT represents the single-population model with independent intrinsic misalignment. TWO¹–INDEPENDENT and TWO²–INDEPENDENT represent the two populations in the two-population model with independent intrinsic misalignment. SINGLE-W14, TWO – W14¹ and TWO – W14² represent the single-population model and the two components of the two-population model with the [Weijmans et al. \(2014\)](#) intrinsic misalignment. $\mu_{\psi_{\text{int}}}$ and $\sigma_{\psi_{\text{int}}}$ are in radians.

| model | μ_{ζ} | σ_{ζ} | μ_{η} | σ_{η} | $\mu_{\psi_{\text{int}}}$ | $\sigma_{\psi_{\text{int}}}$ | f_1 |
|-----------------------------------|------------------------|------------------------|------------------------|------------------------|---------------------------|------------------------------|------------------------|
| SR SINGLE – INDEPENDENT | $0.99^{+0.01}_{-0.02}$ | $0.03^{+0.03}_{-0.01}$ | $0.74^{+0.02}_{-0.01}$ | $0.08^{+0.01}_{-0.01}$ | $0.14^{+0.58}_{-0.40}$ | $4.66^{+1.13}_{-1.26}$ | - |
| NR SINGLE – INDEPENDENT | $0.83^{+0.04}_{-0.06}$ | $0.13^{+0.03}_{-0.03}$ | $0.99^{+0.03}_{-0.04}$ | $0.04^{+0.04}_{-0.03}$ | $0.07^{+0.57}_{-0.44}$ | $0.87^{+1.28}_{-1.35}$ | - |
| SR TWO ¹ – INDEPENDENT | $0.99^{+0.05}_{-0.24}$ | $0.04^{+0.49}_{-0.06}$ | $0.78^{+0.12}_{-0.07}$ | $0.10^{+0.52}_{-0.03}$ | $0.35^{+0.63}_{-0.32}$ | $0.24^{+0.32}_{-0.64}$ | $0.55^{+0.45}_{-0.42}$ |
| SR TWO ² – INDEPENDENT | $0.86^{+0.06}_{-0.20}$ | $0.08^{+0.45}_{-0.06}$ | $0.82^{+0.14}_{-0.06}$ | $0.04^{+0.49}_{-0.03}$ | $1.55^{+0.74}_{-0.39}$ | $0.92^{+0.35}_{-0.57}$ | - |
| NR TWO ¹ – INDEPENDENT | $0.99^{+0.08}_{-0.21}$ | $0.04^{+0.49}_{-0.06}$ | $0.88^{+0.06}_{-0.25}$ | $0.13^{+0.50}_{-0.07}$ | $0.48^{+0.59}_{-0.41}$ | $0.10^{+0.39}_{-0.52}$ | $0.58^{+0.63}_{-0.13}$ |
| NR TWO ² – INDEPENDENT | $0.78^{+0.07}_{-0.19}$ | $0.09^{+0.40}_{-0.05}$ | $0.91^{+0.05}_{-0.21}$ | $0.05^{+0.51}_{-0.06}$ | $1.22^{+0.60}_{-0.38}$ | $1.09^{+0.37}_{-0.45}$ | - |
| SR SINGLE – W14 | $0.99^{+0.01}_{-0.01}$ | $0.13^{+0.01}_{-0.01}$ | $0.82^{+0.03}_{-0.02}$ | $0.12^{+0.03}_{-0.02}$ | - | - | - |
| SR TWO – W14 ¹ | $0.99^{+0.05}_{-0.19}$ | $0.05^{+0.27}_{-0.06}$ | $0.75^{+0.15}_{-0.10}$ | $0.08^{+0.03}_{-0.02}$ | - | - | $0.70^{+0.44}_{-0.47}$ |
| SR TWO – W14 ² | $0.78^{+0.02}_{-0.18}$ | $0.08^{+0.09}_{-0.07}$ | $0.96^{+0.15}_{-0.08}$ | $0.05^{+0.09}_{-0.04}$ | - | - | - |

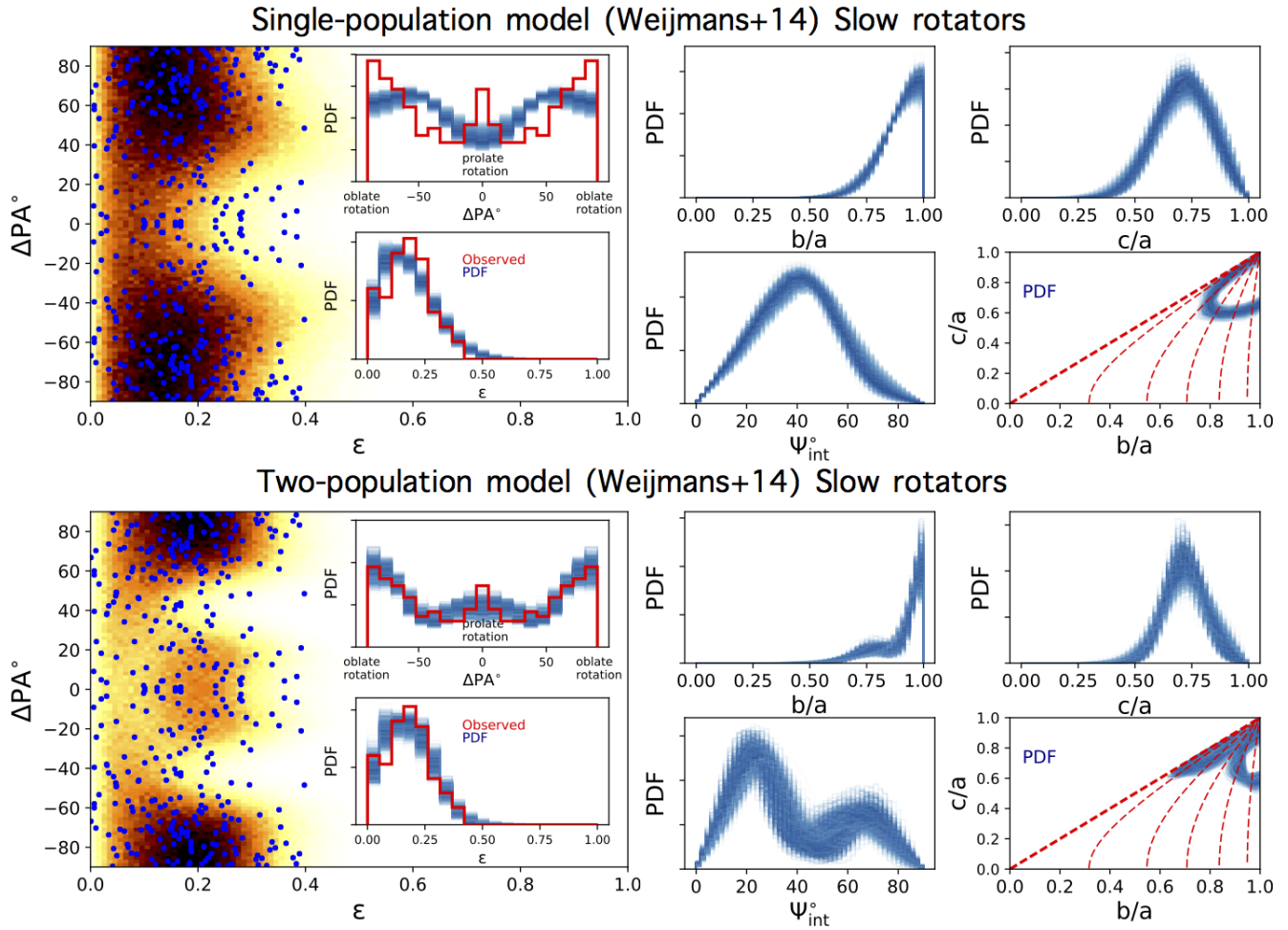


Figure 4. Single-population (top) and two-population (bottom) models with the Weijmans+14 intrinsic misalignment for slow rotators. The other labels and legends are the same as Fig. 2.

distribution (Bundy et al. 2015). Since the galaxies we selected have a narrow mass range (between $2 \times 10^{11} M_{\odot}$ and $\sim 10^{12} M_{\odot}$), this would only have a minor effect on the conclusions.

This work was supported by the National Science Foundation of China (Grant No. 11333003, 11390372 to SM). MC acknowledges support from a Royal Society University Research Fellowship. We performed our computer runs on the Zen high performance computer cluster of the National Astronomical Observatories, Chinese Academy of Sciences (NAOC), and the Venus server at Tsinghua University. This research made use of Marvin (Cherinka et al. 2018), a core Python package and web framework for MaNGA data, developed by Brian Cherinka, José Sánchez-Gallego, and Brett Andrews (MaNGA Collaboration, 2017).

Funding for the Sloan Digital Sky Survey IV has been provided by the Alfred P. Sloan Foundation, the U.S. Department of Energy Office of Science, and the Participating Institutions. SDSS-IV acknowledges support and resources from the Center for High-Performance Computing at the University of Utah. The SDSS web site is www.sdss.org.

SDSS-IV is managed by the Astrophysical Research Consortium for the Participating Institutions of the SDSS Collaboration including the Brazilian Participation Group, the Carnegie Institution for Science, Carnegie Mellon University, the Chilean Participation Group, the French Participation Group, Harvard-Smithsonian Center for Astrophysics, Instituto de Astrofísica de Canarias, The Johns Hopkins University, Kavli Institute for the Physics and Mathematics of the Universe (IPMU) / University of Tokyo, Lawrence Berkeley National Laboratory, Leibniz Institut für Astrophysik Potsdam (AIP), Max-Planck-Institut für Astronomie (MPIA Heidelberg), Max-Planck-Institut für Astrophysik (MPA Garching), Max-Planck-Institut für Extraterrestrische Physik (MPE), National Astronomical Observatories of China, New Mexico State University, New York University, University of Notre Dame, Observatório Nacional / MCTI, The Ohio State University, Pennsylvania State University, Shanghai Astronomical Observatory, United Kingdom Participation Group, Universidad Nacional Autónoma de México, University of Arizona, University of Colorado Boulder, University of Oxford, University of Portsmouth, University of Utah, University of Virginia, University of Washington, University of Wisconsin, Vanderbilt University, and Yale University.

REFERENCES

- Abolfathi, B., Aguado, D. S., Aguilar, G., et al. 2017, ArXiv e-prints, arXiv:1707.09322
- Binney, J. 1985, MNRAS, 212, 767
- Binney, J., & de Vaucouleurs, G. 1981, MNRAS, 194, 679
- Bundy, K., Bershad, M. A., Law, D. R., et al. 2015, ApJ, 798, 7
- Cappellari, M. 2016, ARA&A, 54, 597
- Cappellari, M., Emsellem, E., Bacon, R., et al. 2007, MNRAS, 379, 418
- Cappellari, M., McDermid, R. M., Alatalo, K., et al. 2013a, MNRAS, 432, 1862
- Cappellari, M., Scott, N., Alatalo, K., et al. 2013b, MNRAS, 432, 1709
- Cherinka, B., Sánchez-Gallego, J., Andrews, B., & Brownstein, J. 2018, sdss/marvin: Marvin Beta 2.2.0, , doi:10.5281/zenodo.1146705. <https://doi.org/10.5281/zenodo.1146705>
- Emsellem, E., Cappellari, M., Krajnović, D., et al. 2007, MNRAS, 379, 401
- Emsellem, E., Cappellari, M., Krajnović, D., et al. 2011, MNRAS, 414, 888
- Fasano, G., & Vio, R. 1991, MNRAS, 249, 629
- Fogarty, L. M. R., Scott, N., Owers, M. S., et al. 2015, MNRAS, 454, 2050
- Foreman-Mackey, D., Hogg, D. W., Lang, D., & Goodman, J. 2013, PASP, 125, 306
- Foster, C., van de Sande, J., D’Eugenio, F., et al. 2017, MNRAS, 472, 966
- Franx, M. 1988, MNRAS, 231, 285
- Franx, M., Illingworth, G., & de Zeeuw, T. 1991, ApJ, 383, 112
- Graham, M. T., Cappellari, M., Li, H., et al. 2018, MNRAS, arXiv:1802.08213
- Gunn, J. E., Siegmund, W. A., Mannery, E. J., et al. 2006, AJ, 131, 2332
- Kimm, T., & Yi, S. K. 2007, ApJ, 670, 1048
- Krajnović, D., Emsellem, E., den Brok, M., et al. 2018, ArXiv e-prints, arXiv:1802.02591
- Krajnović, D., Emsellem, E., Cappellari, M., et al. 2011, MNRAS, 414, 2923
- Lambas, D. G., Maddox, S. J., & Loveday, J. 1992, MNRAS, 258, 404
- Li, H., Li, R., Mao, S., et al. 2016, MNRAS, 455, 3680
- Li, H., Mao, S., Emsellem, E., et al. 2018a, MNRAS, 473, 1489
- Li, H., Mao, S., Cappellari, M., et al. 2018b, MNRAS, arXiv:1802.01819
- Ryden, B. 1992, ApJ, 396, 445

- Sandage, A., Freeman, K. C., & Stokes, N. R. 1970, *ApJ*, 160, 831
- Schaller, M., Frenk, C. S., Bower, R. G., et al. 2015, *MNRAS*, 452, 343
- Stark, A. A. 1977, *ApJ*, 213, 368
- Statler, T. S. 1987, *ApJ*, 321, 113
- Tsatsi, A., Lyubenova, M., van de Ven, G., et al. 2017, *A&A*, 606, A62
- Velliscig, M., Cacciato, M., Schaye, J., et al. 2015, *MNRAS*, 453, 721
- Weijmans, A.-M., de Zeeuw, P. T., Emsellem, E., et al. 2014, *MNRAS*, 444, 3340